POLITECNICO DI TORINO
Repository ISTITUZIONALE

Numerical Study of Unsteady Rotating Structures in a Turbine Disk Cavity

Original
Numerical Study of Unsteady Rotating Structures in a Turbine Disk Cavity / Nacci, T., Salvadori, S., Misul, D.A.. - ELETTRONICO. - Volume 6: Heat Transfer: General Interest/ Additive Manufacturing Impacts on Heat Transfer; Heat Transfer: Internal Air Systems; Heat Transfer: Internal Cooling; Industrial & Cogeneration:(2025), pp. 1-12. (ASME Turbo Expo 2025 Turbomachinery Technical Conference and Exposition Memphis, Tennessee (USA) 16-20/06/2025) [10.1115/GT2025-153106].

Availability:
This version is available at: 11583/3001338 since: 2025-08-28T18:25:55Z

Publisher:
American Society of Mechanical Engineers

Published
DOI:10.1115/GT2025-153106

Terms of use:

This article is made available under terms and conditions as specified in the corresponding bibliographic description in the repository

Publisher copyright
ASME postprint/Author's accepted manuscript

(Article begins on next page)

14 September 2026

Proceedings of ASME Turbo Expo 2025
Turbomachinery Technical Conference and Exposition
GT2025
June 16-20, 2025, Memphis, Tennessee

Attendee Read-Only Copy

GT2025-153106

NUMERICAL STUDY OF UNSTEADY ROTATING STRUCTURES IN A TURBINE DISK CAVITY

Teodosio Nacci, Simone Salvadori[1], Daniela Anna Misul

Politecnico di Torino, Corso Duca degli Abruzzi, 24 – 10129 Torino (TO), Italia

ABSTRACT

The improvement of modern cooling systems in aero-engines has led to an increase in the turbine inlet temperature to improve cycle efficiency. In particular, the use of purge flow within the cavity between the stator rim and rotor platform has considerably reduced hot gas ingestion from the main flow and has ensured the maximum metal components operating life. The mechanisms governing axial turbine rim seal flow are complex and influenced by various factors, firstly by the geometry of the cavity. The resulting flow has a three-dimensional structure and a pattern that varies over time. For a wide axial cavity, hot gas ingestion zones can be mainly attributed to three phenomena. The first one is the disc pumping effect generated by the shaft rotation, which induces a radial outflow in the rotor disc boundary layer, creating a recirculation within the cavity that leads to ingestion in the stator disc area. The second one is the vane/blade relative position, which determines a circumferential pressure profile where the higher and lower pressure zones define the flow ejection or ingestion. The third phenomenon is the purge/mainstream flow interaction and its inherent instability that leads to large-scale unsteady flow features developing within the cavity. The formation of such rotating structures and their impact on the ingestion zones is a key research topic in this area. This study presents the results of unsteady numerical simulations (URANS) of an axial turbine's first-stage cavity with a focus on the analysis of 3D-unsteady flow structures. The simulations have been performed by imposing a circumferential pressure periodicity at the outlet, extracted from previous simulations of the stage. The static pressure values within the cavity have been validated by comparison with experimental data. Three purge flow rates have been tested, namely high purge, low purge, and ingestion flow. The paper provides a new perspective on the topic by performing a SPOD analysis on a characteristic plane to identify the main energy modes that dominate the flow and their influence on the ingestion phenomenon.

Keywords: High-Pressure Turbine, Cavity Flows, Unsteady Flows, Computational Fluid dynamics

NOMENCLATURE

ax	axial
b	outer rim radius
$C_p = \frac{p}{{p_1}^o}$	non-dimensional pressure in the cavity
c_s, c_r	stator chord, rotor chord
$C_w = \frac{\dot{m}_0}{\mu * b}$	non-dimensional seal flow rate
f	frequency
$G_c = \frac{s_c}{b}$	axial seal clearance ratio
$\dot{m}_0$	purge air mass flow
N	number of structures
p	static pressure
${p_1}^o$	stator inlet total pressure
r	radius
Re	Reynolds number
s_c	axial seal clearance
T	temperature
V_r	radial velocity
V_c	circumferential velocity
μ	dynamic viscosity of seal flow
Ω	angular disc speed
θ	angle
Δt	time step

ACRONYMS

CFD	computational fluid dynamic
DTF	discrete Fourier tranform
GCI	grid convergence index
LES	large eddy simulation

[1] Corresponding author: simone.salvadori@polito.it

Copyright © 2025 by ASME

POD	proper orthogonal decomposition
ROC	range of convergence
RTT	Reynolds transport theorem
SPOD	spectral proper orthogonal decomposition
SST	shear stress transport
TCF	turbine center frame
TE	trailing edge

1. INTRODUCTION

In turbine stages, shaft rotation relative to the stator vane is realized through a gap between the two parts. This gap corresponds to a cavity, which is subject to ingestion of flow coming from the mainstream. The extraction of cooler flow, named purge flow, from the compressor and its introduction into the cavity prevents the ingestion of hot gases and protects metal components from thermal stresses. The confluence between the two flows is the genesis of a zone where flow is three-dimensional, time-dependent, and strongly non-stationary.

Chew et al. [1] and Scobie et al. [2] highlighted the three main mechanisms that result in ingestion into the cavity. Shaft rotation generates a centrifugal effect such that purge flow exits the cavity into the area of the rotor boundary layer. The occurrence of a radial gradient within the cavity results in lower pressure zones than the mainstream, causing ingestion [3]. The disk pumping effect is responsible for rotationally driven ingestion (RI). Chew [4] quantified the inflow in the RI case through a mathematical model based on momentum integral methods, which he then validated on experimental results. Nketia et al. [5] focused on the RI effect performing LES simulations around an axial seal in a rotor–stator configuration without vanes and blades. They highlighted how Kelvin-Helmholtz instability creates a wavy shear layer that causes the formation of alternating regions of high and low pressure around the rotor side of the seal. The presence of these regions causes ingestion on the rotor side of the seal, although egress starts on the rotor side because of disk pumping effect. Graikos et al. [6] presented a computational, experimental, and theoretical modeling study of RI ingress with CFD predictions of effectiveness. The study proposes an approach for predicting flow rates and flow structures, emphasizing that the cavity flow structure is determined by four key parameters: the sealing flow rate, the swirl of the sealing flow, the ingress mass flow rate, and the swirl of the ingress mass flow rate.

The externally induced input (EI) mechanism focuses on the external flow in the annulus and the dependence of the pressures generated by the relative position of the rotor blade to the stator vane. The emergence of a variable circumferential pressure profile dictated by blade motion generates, at the cavity exit, higher pressure zones where ingress occurs and lower pressure zones where ejection occurs. Abe et al. [7] first isolated the phenomenon experimentally and tested various seal geometries, concluding that the ratio of the cavity to mainstream flow, rim-seal shape, and clearance are the three main factors determining ingestion. Phadke et Owen [8] used blockages in the outer part of the annulus to create different circumferential pressure profiles and, for the various cases, calculated the flow rate of cold flow needed to prevent ingestion by considering the pressure ratio between the inside and outside of the cavity. Gentilhomme et al. [9] experimentally quantified the ingestion of hot flow into the cavity and later concluded that variations in blade and seal geometry affect the zones of flow ingress. Nketia et al. [10] also performed LES simulations to study how the EI effect impact ingress and egress. When RI and EI both play a significant role in hot flow ingestion, combined ingress (CI) occurs. Owen [11] solved the incompressible equations for a simple orifice model in the CI case to calculate the minimum sealing flow rate and correlate it to the sealing effectiveness. The same model was used by Scobie et al. [2] and compared with experimental results. Subsequently, Savov and Atkins [12] showed that shear layer instabilities between the rim seal and mainstream flows influence ingestion and fitted their model to experimental data in the CI case.

The third mechanism concerns the emergence of large-scale rotating structures in the wheel space and rim seal generated by the interaction between purge and mainstream flows. Rotating flow modes rotate at velocities lower than disk one and have an inherently unstable nature. Cao et al. [13] first proved computationally and experimentally the existence of these structures and concluded that they are independent of blade-passing events. In addition, they showed that as the axial gap decreases, there is a reduction in the length scale and strength of the unsteady flow features. Subsequently, several authors confirmed the existence of these structures. In their study, Jakoby et al. [14] and Boudet et al. [15] pointed out that increasing the purge flow rate tends to inhibit the emergence of such structures due to a stronger centrifugal flow and that this cold flow limit varies with the seal configuration. Increased purge flow not only inhibits the formation of such structures but results in increased flux entry into the mainstream with an impact on aerodynamics and intensification of heat transfer on the rotor hub or on the TCF surface, as demonstrated by Jagerhofer et al. [16]. Through an experimental study, Choi et al. [17] realized a linear equation useful, during preliminary turbine cooling design processes, to predict the sealing effectiveness of the rim seal varying the coolant flow rates and rotational Reynolds number. Liu et al. [18] found out how the blades on the rotor have a minimal effect on the pressure distribution downstream of the stator vanes but upstream of the rim seal. They highlighted how RANS can predict the pressure distribution induced by the stator vanes with reasonable accuracy but not the ingress inside the wheelspace. Schädler et al. [19] proved that the presence of hub cavity modes is related to the mechanism of aerodynamic pressure losses in the rotor blade. Julien et al. [20] also observed a varying number of large flow structures in their study, but only for the cases with no and low purge flow, while in the cases with high purge flow, they did not identify any obvious flow perturbations. Gao et al. [21] associated such structures with the phenomenon of inertial waves.

The literature review indicates how the number of structures is variable, not easily predictable, and mainly dependent on the geometry of the cavity and seal, the purge flow rate injected into the cavity, and the axial gap. Consequently, a computational

Copyright © 2025 by ASME

analysis is valuable for predicting the potential occurrence of such unstable phenomena. URANS simulations for axial seal flows have revealed a good ability to capture the phenomenon [13][14] at a significantly lower computational cost than LES simulations. O'Mahoney et al. [22][23] and Gao et al. [24] studied the impact of sector size on the number of structures identified through URANS and LES simulations, concluding that it has an influence, albeit a minimal one, on the visualization of unstable structures and that only when it is significantly smaller than their size does it impact the result more.

This study aims at both identifying and analyzing unstable phenomena in the cavity for three purge flow conditions, namely ingestion of the main flow, low purge (off-design condition), and high purge. Three-dimensional URANS simulations were performed using the commercial software Ansys CFX. The overall accuracy of a detailed analysis of cavity flows performed by considering the cavity geometry subject to unsteady boundary conditions obtained from a 3D simulation of the full stage is determined. The impact of sector size is also considered by comparing a cavity sector of 16.875° and one of 84.375°. Finally, unsteady results are analyzed using Spectral Proper Orthogonal Decomposition (SPOD) to highlight the main energy modes that dominate the flow within the cavity and their frequencies.

Test case description and numerical method are discussed in the first section of the paper. In the second section, after the experimental validation, unsteady numerical results are compared for the three purge flow conditions and two different sector sizes. The energy modes and frequency analysis are discussed in the last section.

2. MATERIALS AND METHODS

2.1 Test case description and test conditions

The object of this study is the axial cavity of the transonic high-pressure turbine stage experimentally investigated at the von Karman Institute for Fluid Dynamics in the compression tube facility [25], consisting of 43 vanes and 64 blades. Experimental and numerical tests provided a full similarity with the engine operating conditions and a Reynolds number at the stator outlet of $Re = 1.1 \cdot 10^6$. The nominal speed of the rotor is Ω = 6500 rpm. The experimental tests also considered an off-design case with a lower rotational speed equal to Ω = 4700 rpm. Details on the experimental campaign, measurement instrumentations, and turbine stage conditions can be found in [25]. The tests were carried out considering three different purge conditions, namely $C_w = 13110$, $C_w = 2638$, and $C_w = -16747$. $C_w = 13110$ holds for the highest input of purge flow (case 1); $C_w = 2638$ refers to the off-design case featuring a slightly lower purge flow (case 2); $C_w = -16747$ represents the ingestion of the hot mainstream flow (case 3). It is worth recalling that the present research specifically addresses the cavity and the related fluid-dynamic phenomena. FIGURE 1(a) shows the geometry of the cavity. The flow enters the cavity through two inlets, a radial one, located in a zone preceded by the bottom labyrinth seals, and axial one, located directly below the stator vanes. In FIGURE 1(b), the two red squares mark the experimental pressure measurement locations. The first is on the stator hub at 0.032×Cs,ax downstream from the vane's TE, while the second is on the cavity stator wall at 0.25×(b-$r_{ax,inlet}$). The cavity has a value of G_c = 0.0048.

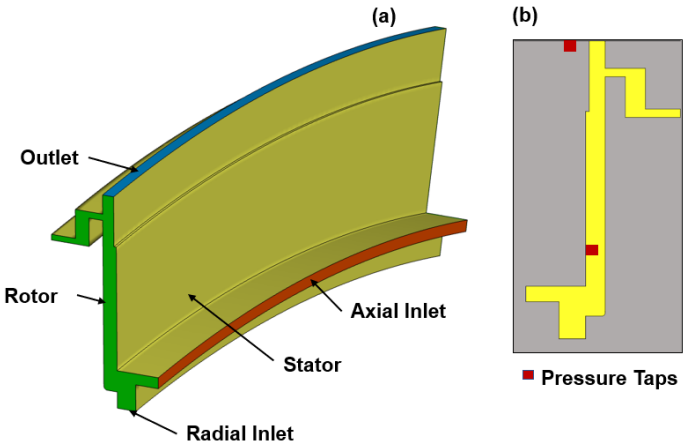

FIGURE 1: (a) 3D VIEW OF THE CAVITY; (b) PRESSURE MEASUREMENT LOCATIONS

2.2 Numerical Method

Computational analysis is the main part of this work and proceeds from a previous numerical study that focused on the first turbine stage. Although the focus of the paper is not on the analysis of the turbine stage, it is fundamental to describe the previous work to properly frame the present research. Unsteady 3D-CFD simulations of the stage were performed using the Reduced Count Ratio (RCR) method proposed by Rai and Madavan [26] and by Dawes [27]. The RCR method takes advantage of domain scaling when there is a non-uniform number of vanes. In this case, a scaling factor of 0.0781 for the blade row was used, allowing the stage to be simulated with a blade count ratio of 2:3 (see FIGURE 2). As proved by Arnone et al. [28], changes by less than 1 percent in the ratio do not significantly affect the results, thus allowing for reducing the computational burden. More information about the performance of the RCR approach with respect to other unsteady methods was highlighted by Salvadori et al. [29].

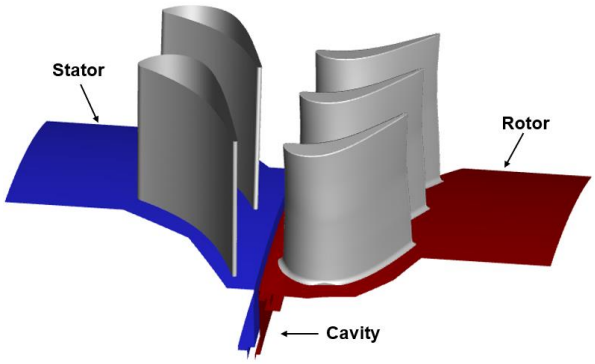

FIGURE 2: 3D VIEW OF THE TURBINE STAGE

Copyright © 2025 by ASME

The simulated cavity extends through an angle of 16.875°, the latter depending on the whole-stage simulations. As a first step, three-dimensional Unsteady Reynolds-Averaged Navier-Stokes (URANS) simulations of both the turbine stage and the cavity were performed using the commercial solver Ansys CFX [30]. The solver employs an implicit spatial discretization method based on the finite volume approach. For the advection terms, a High-Resolution Scheme is used, which dynamically adjusts between first-order upwind and second-order upwind schemes to minimize numerical diffusion while ensuring stability. The temporal discretization follows a second-order accurate scheme, specifically a Backward Euler method, which provides a good balance between accuracy and numerical stability. The time step Δt is chosen as 1/60 of the blade passing time, ensuring an adequate temporal resolution of the flow field. Given that a time-dependent boundary condition is applied at the outlet, the solution does not converge to a steady state. At each timestep, residuals are reduced by at least two orders of magnitude to guarantee numerical accuracy. Additionally, characteristic flow properties (e.g. pressure) are monitored to ensure consistent physical trends over time. To accurately capture turbulent effects, the k-ω Shear Stress Transport (SST) turbulence model [31] is employed. Such model combines the advantages of both the k-ω and k-ε formulations, improving accuracy in predicting flow separation and near-wall behavior.

The mesh used for cavity simulations is hybrid unstructured and consists of prismatic elements in the wall regions and tetrahedra in the core region. The grid uses 18 prismatic layers, with a resulting y^+ value lower than 1 for all the walls in the domain, in accordance with the SST turbulence model.

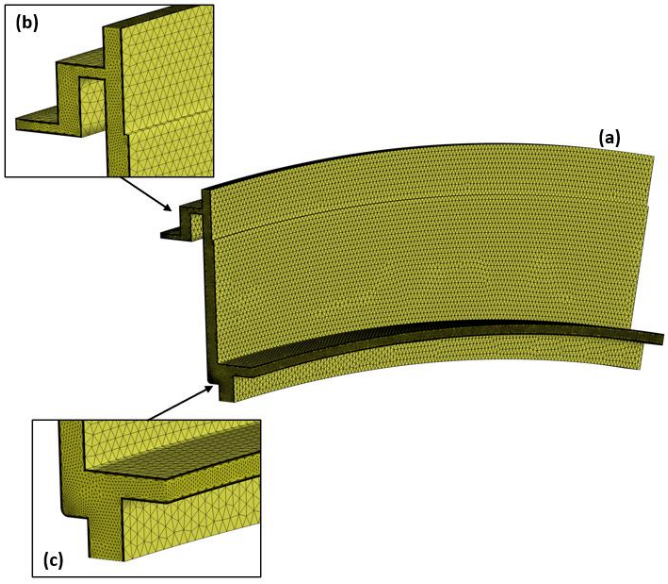

FIGURE 3: (a) 3D VIEW OF THE CAVITY GRID; (b) ZOOM OF THE PERIODICAL FACE; (c) ZOOM OF THE AXIAL INLET GRID

FIGURE 3 shows the adopted grid consisting of about 4 million elements. A mesh independence analysis was performed to prove the absence of influence of spatial discretization and the reliability of the results from the adopted grid. TABLE 1 shows the results through Roache's method [32] for the ratio of the static pressure to the total one at the stage inlet and for the total temperature, on a plane located at 0.5*(b-$r_{ax,inlet}$). The base grid with 4 million elements is compared to two other grids, uniformly scaled in three directions by varying the characteristic length of the tetrahedral elements from the base one, namely a coarse one and a fine one, with 3 million and 7.6 million elements, respectively. Since no relevant differences were found in the results, the base grid was chosen to perform the calculations.

	Grid Step	Refinemnet Ratio	GCI	ROC
$\frac{P}{P_1^o}$	Coarse-Medium	1.34	0.022%	1.0004
	Medium-Fine	1.24	0.015%	
T^o	Coarse-Medium	1.34	0.074%	1.0003
	Medium-Fine	1.23	0.021%	

TABLE 1: GRID INDEPENDENCE QUANTIFICATION

The same analysis was conducted for the overall stage simulations, resulting in a 26.5 million elements mesh. In addition, simulations were performed with a larger angular cavity sector, respecting the circumferential periodicity of the static pressure boundary conditions. A sector of 84.375° (5 times 16.875°) was finally selected and the mesh was adapted to the domain, consistently multiplying its elements by 5.

2.3 Boundary Conditions

The present section provides a detailed discussion of the adopted boundary conditions for cavity simulation. Firstly, it is appropriate to highlight the imposed boundary conditions for the whole-stage simulations. The imposed stage inlet total pressure is P_{01}=1.59 bar and inlet total temperature is T_{01}=442 K. The stage pressure ratio is P_{01}/P_{s3}=3.12. Concerning the simulations of the cavity, the inlet boundary conditions are mass flow rate and total temperature imposed at the two cavity inlets highlighted in FIGURE 1(b). The relative total temperature of the coolant entering the cavity is 295 K. This value applies to the two radial and axial inlets (see TABLE 2) by considering the contribution of the kinetic term from the Reynolds Transport Theorem (RTT). Indeed, such a term represents the contribution of the circumferential velocity to the total enthalpy of the inlet flow and results in an increase or decrease in the total temperature imposed at the inlet of the domain, depending on whether the flow enters the cavity radially or axially. This ensures a realistic energy balance in the rotating system. The numerical C_w values for the three simulations are the same as the experiments.

The boundary conditions at the cavity outlet derive directly from the 3D stage simulations. In the whole-stage simulations,

Copyright © 2025 by ASME

axially averaged pressure profiles at the cavity outlet are extracted for each time step composing a period. The extracted pressure profiles highlight the circumferential pressure variation considering the relative position of the blades at each time step. Since the same time step is used in both the whole-stage and cavity simulations, and the cavity domain is modeled in the rotating reference frame in both cases, instantaneous static pressure profiles extracted from the whole-stage simulations are directly applied at the same location in the cavity simulations.

At the cavity outlet an "Opening" boundary condition is used, allowing both outflow and inflow depending on the local pressure gradients. When the flow exits the domain, the applied boundary condition corresponds to a static pressure value. Conversely, if the flow reverses and enters the domain, the solver considers a total pressure value obtained from the imposed static pressure and the contribution of the normal velocity component. This approach ensures a more realistic treatment of possible flow recirculation at the domain outlet. In the case where the flow enters the domain at the outlet zone, the solver requires a static flow inlet temperature. The static temperature is derived from the whole-stage simulations by considering the circumferential mass-flow weighted average value of the main flow in the stator hub area, at 0.032×Cs,ax downstream from the vane's TE (the same as the pressure tap located at the hub).

C_w	$T^0_{\text{axial inlet}}$ [K]	$T^0_{\text{radial inlet}}$ [K]
13110	271	318
2638	/	307
-16747	/	/

TABLE 2: TEMPERATURE BOUNDARY CONDITIONS

All solid walls within the geometry are treated as isothermal through the imposition of a static temperature of 310 K. In this work, the entire domain is modeled in the rotating reference frame, with the stator wall being assigned a counter-rotating condition to reproduce its stationary behavior in the absolute frame. This approach allows for simulating the domain without using interfaces between the stator and rotor zones and to capture the relative motion between the two parts.

FIGURE 4 shows all the 180 static pressure extracted profiles that compose a simulated period for the ingestion case. Each pressure profile is imposed circumferentially at the outlet over time. FIGURE 5 and FIGURE 6 highlight the extracted profiles for the condition with C_w = 13110 and the off-design case, respectively. Instantaneous static pressure has been normalized to the pressure at the stage inlet, while the x-axis shows the circumferential length of the cavity normalized to its maximum value. In the off-design case, the flow enters the cavity only through the radial inlet, while for the case with C_w = 13110, the flow enters from both inlets. The ingestion case is different because there is an opposite flow direction that results in a hot flow entry into the cavity.

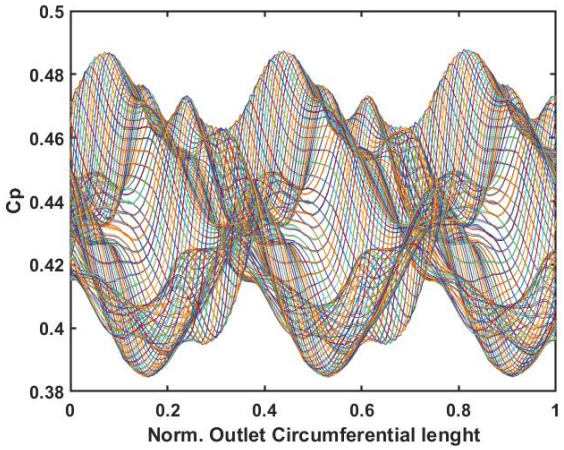

FIGURE 4: CIRCUMFERENTIAL STATIC PRESSURE PROFILES IMPOSED AS BOUNDARY CONDITIONS AT THE CAVITY OUTLET, C_w = -16747

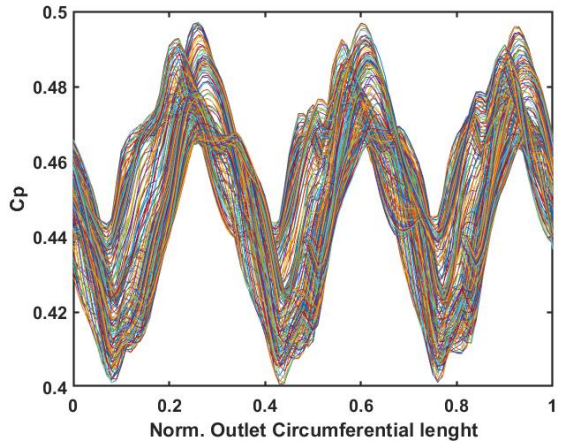

FIGURE 5: CIRCUMFERENTIAL STATIC PRESSURE PROFILES IMPOSED AS BOUNDARY CONDITIONS AT THE CAVITY OUTLET, C_w = 13110

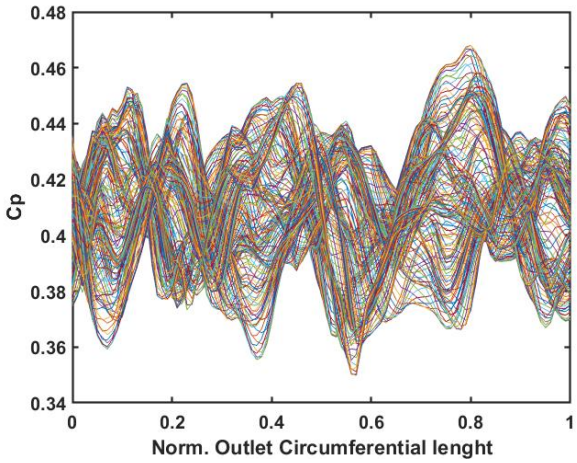

FIGURE 6: CIRCUMFERENTIAL STATIC PRESSURE PROFILES IMPOSED AS BOUNDARY CONDITIONS AT THE CAVITY OUTLET, C_w = 2638

Copyright © 2025 by ASME

2.4 Verification and Validation

This section reports experimental validation for both the stage and cavity simulations. Experimental validation is carried out with static pressure values measured at the two different locations highlighted in FIGURE 1(b). The static pressure time-averaged distribution is obtained considering the values extracted from each time step of a simulated period. In particular, the numerical data from the unsteady whole-stage simulations are compared to the experimental one, in the hub zone located upstream of the cavity at $0.032 \times c_{s,ax}$ downstream from the vane's TE. FIGURE 7 shows C_p values as a function of the vane phase.

Numerical results show a good match in the cases holding the nominal rotational velocity, namely case 1 and case 3. Still, the pressure is higher for ejection case 1 given that the purge flow exiting the cavity generates a local pressure increase as it enters the main flow. The off-design condition (case 2) shows a different and slightly out-of-phase trend to the experimental points. In addition, this condition features the lowest average pressure values.

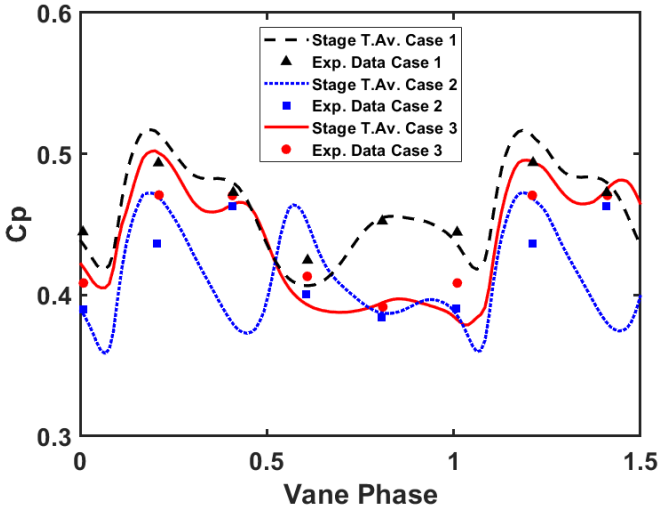

FIGURE 7: TIME-AVERAGED DISTRIBUTION OF PITCH-WISE STATIC PRESSURE AT VANE EXIT HUB

Validation continues inside the cavity through static pressure values measured at the stator wall. FIGURE 8 compares the experimental and numerical C_p values, as a function of the vane phase, in the cases of the whole-stage and cavity-only simulations. The numerical data for both simulations show the same trend and almost perfectly overlap with the sound exception of ingestion occurrence, where the mismatch is anyhow lower than 1%. These results support the reliability of the only-cavity simulations. Moreover, the numerical results replicate the experimental measurements with slight differences. In particular, the two cases with ejection (case 1 and case 2) present slightly lower trends than the experimental ones and a mismatch lower than 5%, whereas the case with flow ingestion (case 3) presents a trend slightly above the experimental data and a mismatch lower than 2.5%.

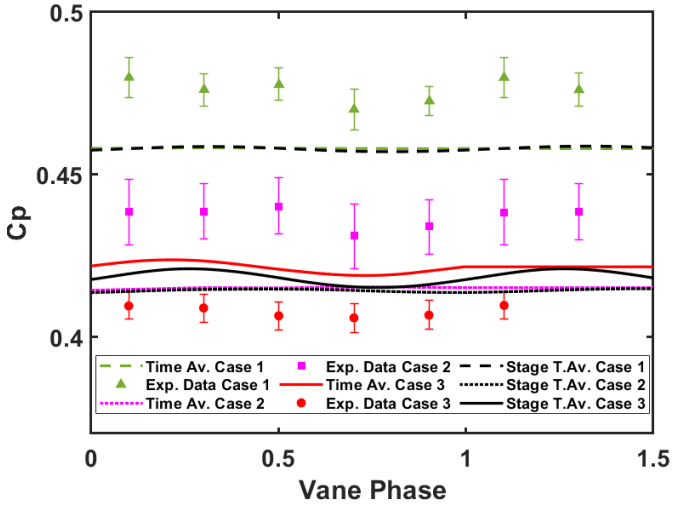

FIGURE 8: TIME-AVERAGED DISTRIBUTION OF PITCH-WISE STATIC PRESSURE INSIDE THE CAVITY

3. RESULTS AND DISCUSSION

The existence and impact of rotating structures within the cavity are investigated through CFD analysis by means of radial velocity plots. This section compares the results of the three different purge flow conditions. The unsteady pressure field is inspected using the SPOD technique that identifies the most energetic modes present in the cavity by associating them with specific frequencies.

3.1 Flow structures

The presence and occurrence of flow structures within the axial gap between the rotating and stationary zones is shown on a plane (see FIGURE 9) located at half the axial distance between the two cavity walls ($0.5*s_c$). FIGURE 10 and FIGURE 11 show the instantaneous normalized radial velocity field for the three considered purge flow conditions, for the 16.875° and 84.375° sectors, respectively. The number of structures shown in TABLE 3 is calculated, for both considered sectors, using equation (1):

$$N_{360^\circ} = N_\theta * \frac{360^\circ}{\theta} \quad (1)$$

C_w	N_{360° (16.875°)	N_{360° (84.375°)
13110	64	64
2638	85	85
-16747	43	43

TABLE 3: NUMBER OF STRUCTURES

The most evident result is the independence of the total number of structures from the angle of the simulated sector. This result is in line with the findings of O'Mahoney et al. [22][23]

Copyright © 2025 by ASME

and Gao et al. [24], stating that the sector angle has a direct impact on the result when it is small if compared to the size of the structures. In this case, the cavity features a simple geometry, a small axial gap, and several structures. This observation is consistent with Cao et al. [13], showing that axial cavities with small gaps have unstable structures with a smaller length scale.

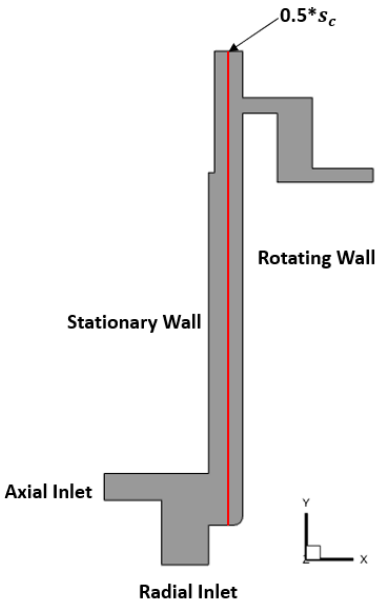

FIGURE 9: REFERENCE PLANE

The case with ingestion (see FIGURE 10(c) and FIGURE 11(c)) presents the lowest number of structures. This case shows a clear ingress of hot flow from the mainstream into the cavity, which is evident from the negative radial velocity values on the investigation plane. The condition with C_w = 13110 (case 1) (see FIGURE 10 (a) and FIGURE 11 (a)) shows structures closer to the cavity outlet and the highest homogeneity of radial velocity distribution in the central zone among the three cases. Such behavior is to be ascribed to the injection of a higher amount of purge flow with respect to the other two cases. Increasing the value of $\dot{m}_0$ pushes these structures closer to the outlet. The off-design case (see FIGURE 10 (b) and FIGURE 11 (b)) is the most interesting, because the amount of cold flow entering the cavity is lower, allowing for a clearer visualization of the phenomenon. These structures have a greater radial extent than in the high purge flow case.

The off-design condition (case 2) has the highest number of structures (85) because of the lower cold flow injected and lower angular velocity. The shapes of the structures vary across the three cases: in the case with C_w = 13110, the structures are flattened toward the outlet; in the off-design case, they extend more and penetrate further into the cavity whereas and in the case with ingestion, the hot flow completely penetrates the radial extent of the cavity. The structures do not maintain a consistent shape, even within a single case; instead, their shapes and positions change dynamically during shaft rotation.

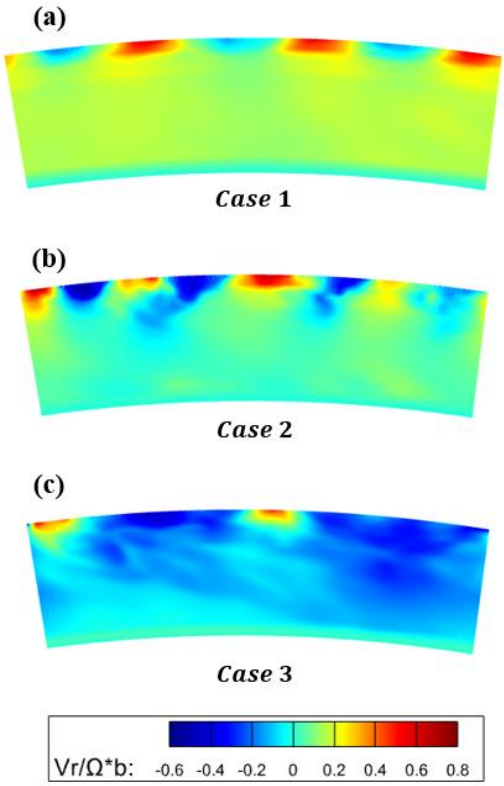

FIGURE 10: INSTANTANEOUS RADIAL VELOCITY CONTOURS FOR THE 16.875° SECTOR, CENTRAL PLANE: (a) C_w = 13110; (b) C_w = 2638; (c) C_w = -16747

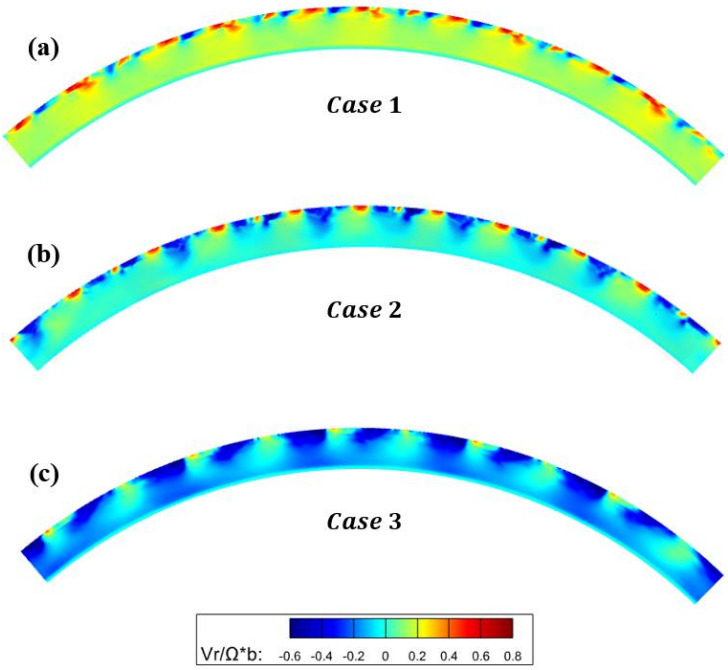

FIGURE 11: INSTANTANEOUS RADIAL VELOCITY CONTOURS FOR THE 84.375° SECTOR, CENTRAL PLANE: (a) C_w = 13110; (b) C_w = 2638; (c) C_w = -16747

Copyright © 2025 by ASME

3.2 SPOD Methodology

Spectral POD is a data analysis technique highlighting oscillating phenomena and their frequencies. This technique has been used in various applications, such as to reveal flow fluctuations in the case of tip leakage vortex in compressors [33] or for a cooling hole [34]. In the present case, SPOD is performed on static pressure. SPOD, (Towne et al. [35], Schmidt and Colonius [36]), differently from the POD, identifies modes that are not only coherent in space but also in time (Lumley [37]). The identification of the modes is performed by processing many representative snapshots of an unsteady phenomenon. Each snapshot represents a vector: $p_i \in R^{N_p \times N_v}$, where N_p represents the number of points in the mesh (in the present case the barycenter of the cells), N_v the number of variables considered (in our case pressure). All vectors are collected in a matrix in chronological order (equation (2)) to have a representation in both time and space:

$$P = [p_1, p_2, \dots p_{N_t}] \in R^{N_T \times N_p} \quad (2)$$

N_T represents the number of snapshots. These snapshots are divided into blocks composed of $N_f < N_T$ snapshots. Then, to visualize the problem in the frequency domain, a Discrete Fourier Transform (DTF) is performed for each block, and each one is overlapped with neighboring blocks so that no information is lost during the analysis. The frequency components are separated to study the dependence of the flow on these frequencies. For each frequency, a spectral covariance matrix is constructed to describe the correlation between the spatial data at that frequency. The spectral covariance matrix is decomposed into eigenvalues and eigenvectors, as explained by [35]. The eigenvalues represent the energy associated with each mode and are decreasingly ordered, while the eigenvectors represent the modes in space and are orthogonal to each other.

3.3 SPOD Results

Frequency analysis is realized for the static pressure variable of the off-design case (case 2). From a set of 12288 timesteps, related to the 16.875° cavity, static pressure values are extracted for the barycenter of the cells in the axial plane considered above, set at $0.5*s_c$. The pressure values are weighted over the areas of the cells to which they belong. FIGURE 12 shows the SPOD spectrum obtained from the analysis. Each line represents a POD mode that combines SPOD modes, which instead consider frequencies. The following analysis focused on the first mode as the most energetic and representative peak.

FIGURE 13 and FIGURE 14 show the module and phase for mode 1 in FIGURE 12. In the SPOD analysis, the most energetic mode (mode 1) is obtained for a frequency $f_1 = 43*\Omega$, where 43 is the number of vanes, which are a periodic source of fluctuations. The rotating reference frame experiences a modulated contribution from the interaction between stator vanes and rotor blades. Tyler and Sofrin [38] provide an in-depth analysis of the modes created by the interaction between the stator and rotor. In FIGURE 13 the mode presents the highest energy values in the area closest to the outlet, reflecting the stator-rotor interaction.

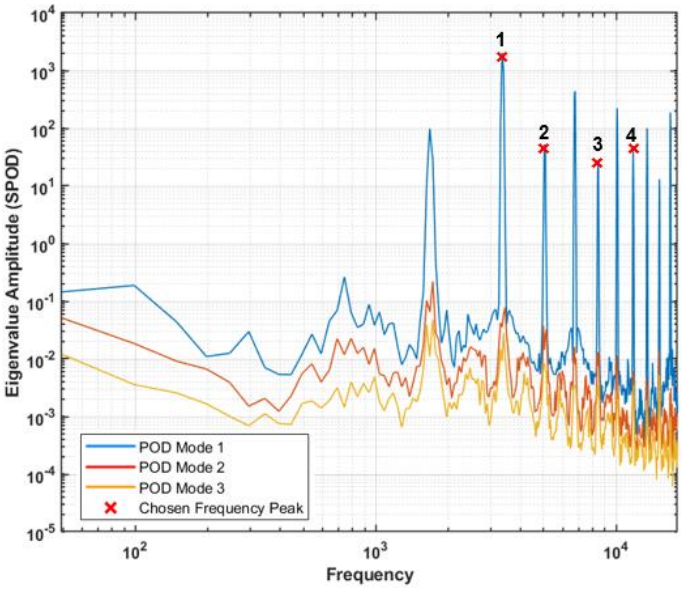

FIGURE 12: SPOD SPECTRA, CENTRAL PLANE

The phase in FIGURE 14 shows the propagation of the phenomenon in the cavity with 3 variations along the circumferential direction. FIGURE 15 highlights the reconstruction of the pressure field signal, normalized to the inlet total pressure of the cavity, at the frequency identified by the mode 1 peak for a time step. This represents the single contribution of mode 1, which is the most energetic, to the reconstruction of the static pressure field for the considered time step. The static pressure field of a single time step in the URANS simulation is the result of the contribution of all modes in the spectrum. The second most interesting mode (mode 2 in FIGURE 12) has a frequency of $f_2 = 64*\Omega$, where 64 is the number of rotor blades. FIGURE 16 and FIGURE 17 show the module and phase for this specific mode, while FIGURE 18 depicts the reconstruction of the pressure field signal.

These two modes (1 and 2) generate a series of higher-order harmonics with pronounced energy peaks, as shown in FIGURE 12. An example is mode 3, which has $f_3 = 107*\Omega$ ($f_3 = f_1 + f_2$) as its characteristic frequency. This mode is the product of an intermodulation process of mode 1 and mode 2. The same applies to mode 4 in FIGURE 12, characterized by a frequency $f_4 = 150*\Omega$ ($f_4 = 2 * f_1 + f_2$). These two modes, although less energetic than other modes, show a circumferentially sinusoidal pattern in the plane central area (see FIGURE 19 and FIGURE 22), with alternating higher and lower energetic zones. The same can be seen for the phase (see FIGURE 20 and FIGURE 23), which shows a similar circumferential pattern.

FIGURE 21 and FIGURE 24 represent the reconstruction of the pressure field signal for mode 3 and mode 4, respectively, normalized with respect to the total inlet pressure of the cavity for the considered frequency. The intermediate peak between mode 2 and mode 3 was not included as it corresponds to the

Copyright © 2025 by ASME

harmonic of mode 1 with f = 2*f_1. Mode 3 and mode 4 were chosen to be displayed as explanatory of the interaction behavior of modes 1 and 2; the remaining peaks are either harmonics or subharmonics of mode 1 or mode 2 or a product of the interaction between modes with lower energy content.

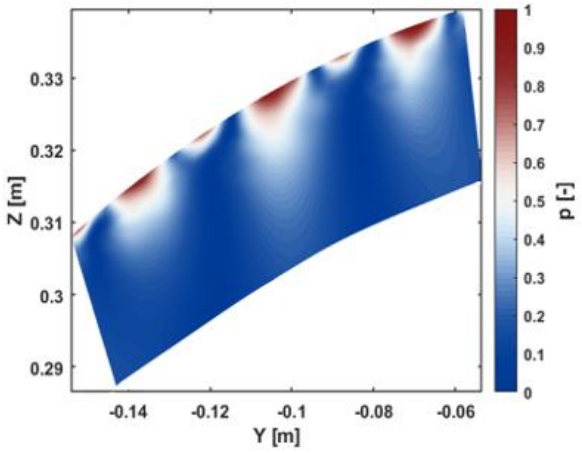

FIGURE 13: MODULE SPOD MODE 1

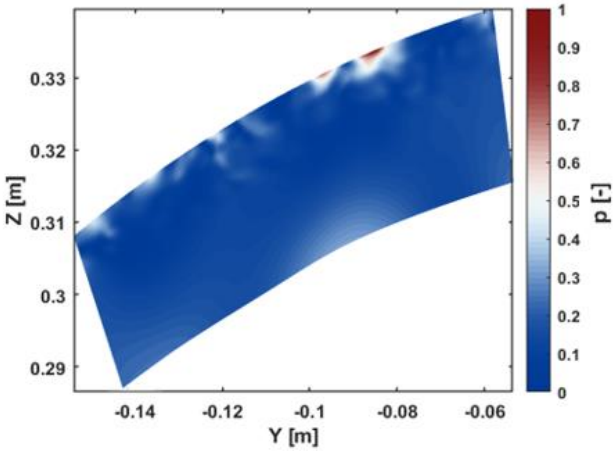

FIGURE 16: MODULE SPOD MODE 2

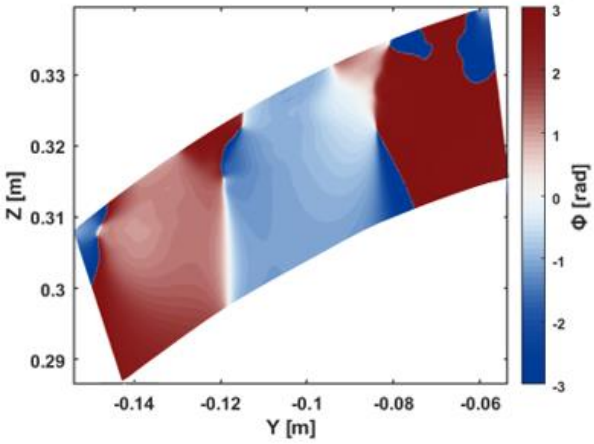

FIGURE 14: PHASE SPOD MODE 1

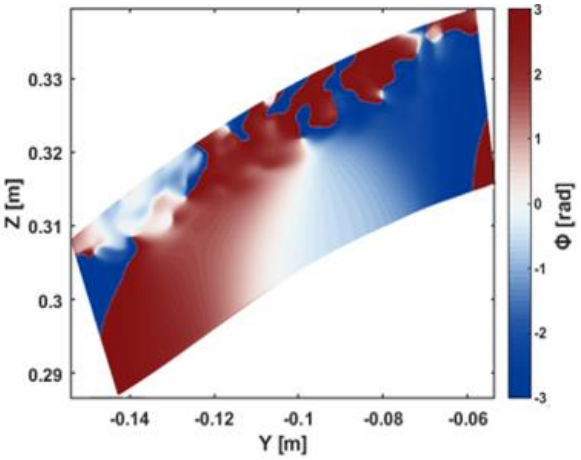

FIGURE 17: PHASE SPOD MODE 2

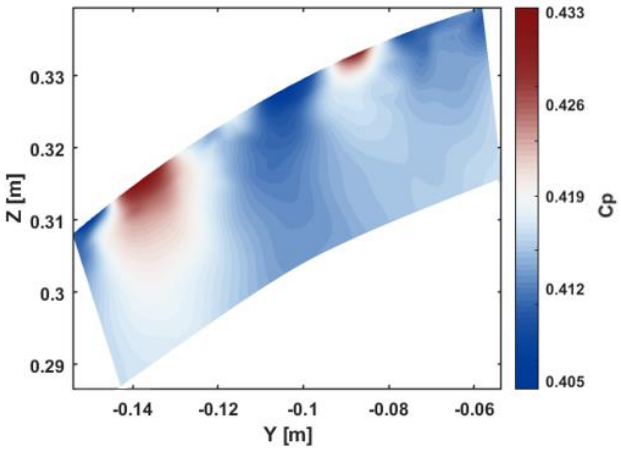

FIGURE 15: INSTANTANEOUS PRESSURE FIELD RECONSTRUCTION, SPOD MODE 1

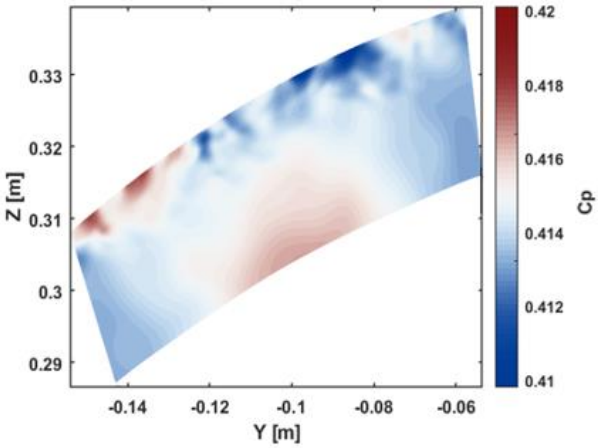

FIGURE 18: INSTNTANEOUS PRESSURE FIELD RECONSTRUCTION, SPOD MODE 2

Copyright © 2025 by ASME

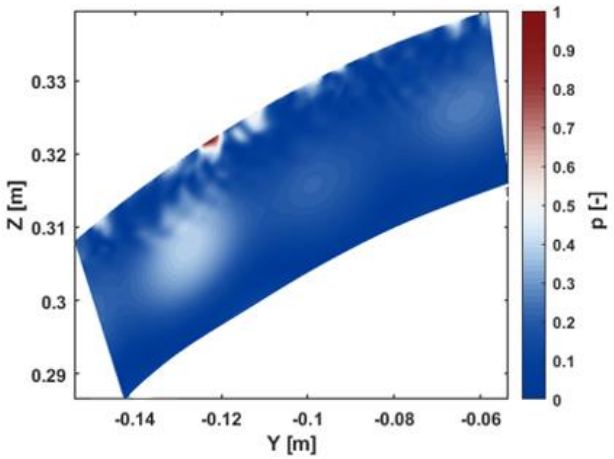

FIGURE 19: MODULE SPOD MODE 3

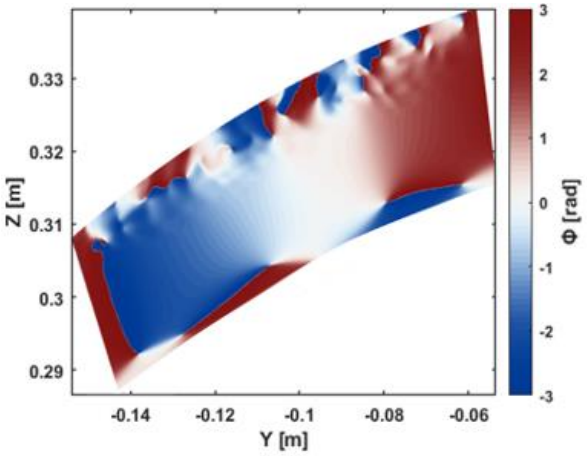

FIGURE 20: PHASE SPOD MODE 3

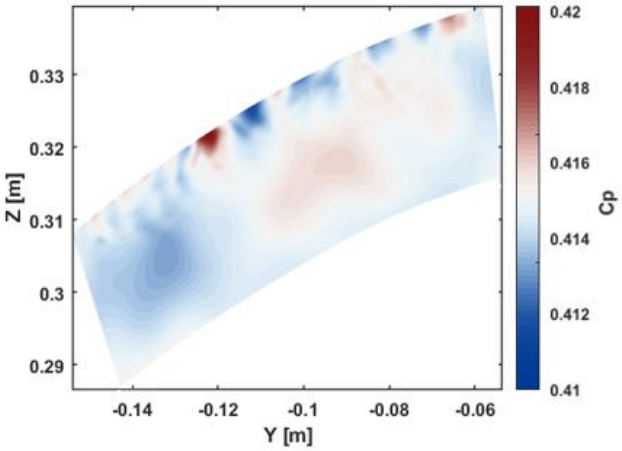

FIGURE 21: INSTANTANEOUS PRESSURE FIELD RECONSTRUCTION, SPOD MODE 3

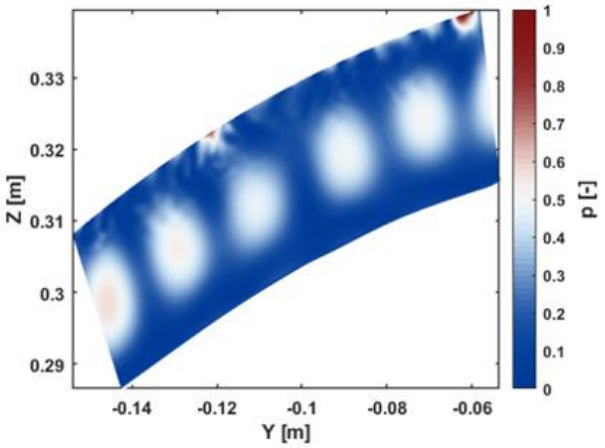

FIGURE 22: MODULE SPOD MODE 4

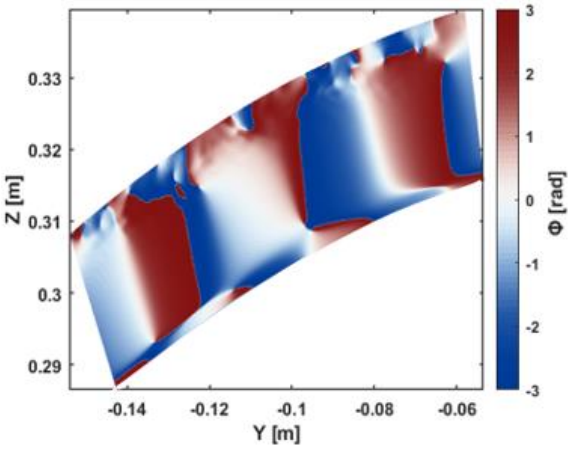

FIGURE 23: PHASE SPOD MODE 4

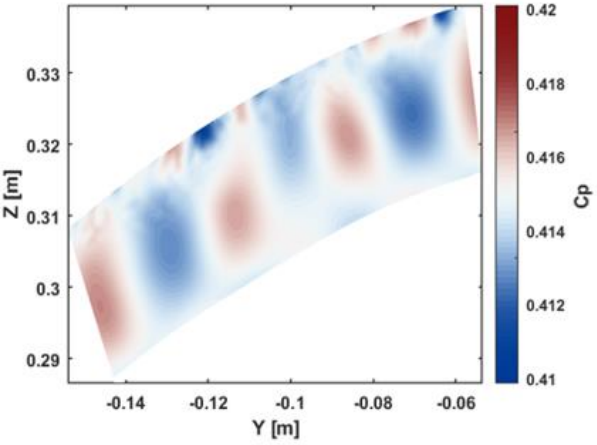

FIGURE 24: INSTANTANEOUS PRESSURE FIELD RECONSTRUCTION, SPOD MODE 4

Copyright © 2025 by ASME

4. CONCLUSIONS

In this paper, a numerical study of the unsteady rotating structures and a frequency analysis of the flow within the cavity between the stator and rotor is performed. The focus is the cavity of an HP first stage with axial clearance geometry. Such analysis is of utmost importance to identify critical conditions that might eventually arise in the cavity to prevent overheating of the metal parts.

Three different purge flow conditions are considered: ingestion of the main flow, low purge (off-design condition), and high purge. The connection of the cavity with the stage is considered through the imposition, at the domain outlet, of static pressure profiles extracted and imported directly from the overall stage simulation. 3D-CFD URANS simulations are performed on a fine mesh. The first part validates the numerical model used for cavity-only simulations by comparing it to experimental data and numerical results of the overall stage simulations.

In the second part, a comparison is carried out for the radial velocity field in an axial plane equally spaced from the stator and rotor wall, for two sectors of 16.875° and 84.375°. The results show the independence of the number of structures identified from the size of the considered sector. The cavity has a small axial gap that generates several unstable structures of limited size. This supports the conclusion that the sector angle directly impacts the result when it is small relative to the size of the structures. The number of structures is different for the three purge flow conditions tested.

The final part of the work involves a frequency analysis performed using SPOD (Spectral Proper Orthogonal Decomposition) on static pressure for the low purge case, in the axial plane at the center of the cavity. This technique reveals the flow fluctuations in detail and identifies the most energetic modes in space and time by placing them in their frequency range. A set of 12288 snapshots is used to perform the analysis, producing a clear frequency spectrum. The most representative and energetic mode (mode 1) is at a frequency of $f_1 = 43*\Omega$, where 43 is the number of vanes. The analysis shows that the interaction of the stator vanes and rotor blades is a periodic source of fluctuations. The second mode considered (mode 2) is at a frequency of $f_2 = 64*\Omega$, where 64 are the rotor blades. The peaks at higher frequencies are higher-order harmonics of modes 1 and 2 or a consequence of the intermodulation process between the two (e.g., modes 3 and 4). The phase and module plots, respectively, identify the energy distribution in the plane, the presence of rotating waves, and their direction of propagation, for the four modes considered. Finally, plots of instantaneous reconstructed pressure related to the analyzed modes provide direct feedback and visualization of a significant physical variable such as pressure.

REFERENCES

[1] Chew JW, Gao F, Palermo DM. Flow mechanisms in axial turbine rim sealing. Proceedings of the Institution of Mechanical Engineers, Part C: Journal of Mechanical Engineering Science. 2019;233(23-24):7637-7657.

[2] Scobie, J. A., Sangan, C. M., Michael Owen, J., and Lock, G. D. (July 27, 2016). "Review of Ingress in Gas Turbines." ASME. J. Eng. Gas Turbines Power. December 2016; 138(12): 120801.

[3] Owen, J. M. (November 12, 2010). "Prediction of Ingestion Through Turbine Rim Seals—Part I: Rotationally Induced Ingress." ASME. J. Turbomach. July 2011; 133(3): 031005.

[4] Chew, J. W., Dadkhah, S., and Turner, A. B. (April 1, 1992). "Rim Sealing of Rotor–Stator Wheelspaces in the Absence of External Flow." ASME. J. Turbomach. April 1992; 114(2): 433–438.

[5] Nketia, Sabina, et al. "Large Eddy Simulation of Rotationally Induced Ingress and Egress around an Axial Seal between Rotor and Stator Disks." Energies 16.11 (2023): 4354.

[6] Graikos, D., Tang, H., Carnevale, M., Bailey, N. Y., & Scobie, J. A. (2024). Rotationally induced ingress in rotor–stator systems. Physics of Fluids, 36(7).

[7] Abe, T. (1979). An investigation of turbine disk cooling (experimental investigation and observation of hot gas flow into a wheel space). In *Proc. 13th CIMAC Congress, Vienna* (pp. GT-30).

[8] U.P. Phadke, J.M. Owen, Aerodynamic aspects of the sealing of gas-turbine rotor-stator systems: Part 3: The effect of nonaxisymmetric external flow on seal performance, International Journal of Heat and Fluid Flow,Volume 9, Issue 2, 1988, Pages 113-117.

[9] Gentilhomme , O., Hills , N. J., Turner, A. B., and Chew, J. W. (August 27, 2003). "Measurement and Analysis of Ingestion Through a Turbine Rim Seal." ASME. J. Turbomach. July 2003; 125(3): 505–512.

[10] Nketia, S., Bryden, K. M., Dalton, R., & Shih, T. I. (2023). Large Eddy Simulation of Externally Induced Ingress about an Axial Seal by Stator Vanes. Energies, 16(16), 5985.

[11] Owen, J. M. (November 12, 2010). "Prediction of Ingestion Through Turbine Rim Seals—Part II: Externally Induced and Combined Ingress." ASME. J. Turbomach. July 2011; 133(3): 031006.

[12] Savov, SS, & Atkins, NR. "A Rim Seal Ingress Model Based on Turbulent Transport." Proceedings of the ASME Turbo Expo 2017: Turbomachinery Technical Conference and Exposition. Volume 5B: Heat Transfer. Charlotte, North Carolina, USA. June 26–30, 2017. V05BT15A009. ASME.

[13] Cao, C., Chew, J. W., Millington , P. R., and Hogg, S. I. (November 24, 2004). "Interaction of Rim Seal and Annulus Flows in an Axial Flow Turbine" ASME. J. Eng. Gas Turbines Power. October 2004; 126(4): 786–793.

[14] Jakoby, R., Zierer, T., Lindblad, K., Larsson, J., deVito, L., Bohn, D. E., Funcke J., Decker, A. (2004, January). Numerical simulation of the unsteady flow field in an axial gas turbine rim seal configuration. In Turbo Expo: Power for Land, Sea, and Air (Vol. 41693, pp. 431-440).

Copyright © 2025 by ASME

[15] Boudet J, Autef VND, Chew JW, Hills NJ, Gentilhomme O. Numerical simulation of rim seal flows in axial turbines. The Aeronautical Journal (1968). 2005;109(1098):373-383.
[16] Jagerhofer, P. R., Glasenapp, T., Patzer, B., and Göttlich, E. (October 15, 2024). "Impact of Blowing and Density Ratio on the Film Cooling and Heat Transfer in an Aggressive Turbine Center Frame." ASME. J. Turbomach. March 2025; 147(3): 031010.
[17] Choi, Seok Min, Seungyeong Choi, and Hyung Hee Cho. "Effect of various coolant mass flow rates on sealing effectiveness of turbine blade rim seal at first stage gas turbine experimental facility." Energies 13.16 (2020): 4105.
[18] Liu, Jason, et al. "Modelling and simulation of ingress into the rim seal and wheelspace of a gas-turbine rotor-stator configuration." 53rd AIAA Aerospace Sciences Meeting. 2015.
[19] Schädler, R., Kalfas, A. I., Abhari, R. S., Schmid, G., and Voelker, S. (September 20, 2016). "Modulation and Radial Migration of Turbine Hub Cavity Modes by the Rim Seal Purge Flow." ASME. J. Turbomach. January 2017; 139(1): 011011.
[20] Julien S, Lefrancois J, Dumas G, et al. Simulations of flow ingestion and related structures in a turbine disk cavity. In: ASME turbo expo, 2010, paper no. GT2010-22729.
[21] Gao, Feng, John W. Chew, and Olaf Marxen. "Inertial waves in turbine rim seal flows." Physical Review Fluids 5.2 (2020): 024802.
[22] O'Mahoney, T. S. D., et al. "Large-eddy simulation of rim seal ingestion." Proceedings of the Institution of Mechanical Engineers, Part C: Journal of Mechanical Engineering Science 225.12 (2011): 2881-2891.
[23] O'Mahoney, T., N. Hills, and J. Chew. "Sensitivity of LES results from turbine rim seals to changes in grid resolution and sector size." Progress in Aerospace Sciences 52 (2012): 48-55.
[24] Gao, Feng, et al. "Advanced numerical simulation of turbine rim seal flows and consideration for RANS turbulence modelling." Turbo Expo: Power for Land, Sea, and Air. Vol. 51098. American Society of Mechanical Engineers, 2018.
[25] Pau, M., Paniagua, G., Delhaye, D., de la Loma, A., and Ginibre, P. (January 11, 2010). "Aerothermal Impact of Stator-Rim Purge Flow and Rotor-Platform Film Cooling on a Transonic Turbine Stage." ASME. J. Turbomach. April 2010; 132(2): 021006.
[26] Rai, Man Mohan, and Nateri K. Madavan. "Multi-airfoil Navier–Stokes simulations of turbine rotor–stator interaction." (1990): 377-384.
[27] Dawes, W. N. "The simulation of three-dimensional viscous flow in turbomachinery geometries using a solution-adaptive unstructured mesh methodology." (1992): 528-537.
[28] Arnone, Andrea, and Roberto Pacciani. "Rotor-stator interaction analysis using the Navier–Stokes equations and a multigrid method." (1996): 679-689.
[29] Salvadori S., Insinna M., Martelli F., 2024. Unsteady Flows and Component Interaction in Turbomachinery. MDPI Int. J. Turbomach. Propuls. Power, Special Issue “Advances in Critical Aspects of Turbomachinery Components and Systems”, Vol 9, Issue 2, No. 15 (65 pages), doi: 10.3390/ijtpp9020015
[30] Ansys CFX-Solver Theory Guide, Release 2022 R2. 2022.
[31] Menter, Florian R. "Two-equation eddy-viscosity turbulence models for engineering applications." AIAA journal 32.8 (1994): 1598-1605.
[32] Roache, Patrick J. "Perspective: a method for uniform reporting of grid refinement studies." (1994): 405-413.
[33] He, Xiao, et al. "Spectral proper orthogonal decomposition of compressor tip leakage flow." Physics of Fluids 33.10 (2021).
[34] Rosafio, N., De Cosmo, G., Salvadori, S., Carnevale, M., & Misul, D. A. (2022, June). Identification of fluctuation modes for a cylindrical film cooling hole using the spectral proper orthogonal decomposition method. In Turbo Expo: Power for Land, Sea, and Air (Vol. 86038, p. V06AT12A006). American Society of Mechanical Engineers.
[35] Towne, A., Schmidt, O. T., and Colonius, T., 2018. “Spectral proper orthogonal decomposition and its relationship to dynamic mode decomposition and resolvent analysis”. Journal of Fluid Mechanics, 847, p. 821–867.
[36] Schmidt, O. T., and Colonius, T., 2020. “Guide to spectral proper orthogonal decomposition”. AIAA Journal, 58(3), pp. 1023–1033.
[37] Lumley, J., 1967. “The structure of inhomogeneous turbulent flows”. Atmospheric Turbulence and Radio Propagation, pp. 166–178.
[38] Tyler, John M., and Thomas G. Sofrin. Axial flow compressor noise studies. No. 620532. SAE Technical Paper, 1962.

Copyright © 2025 by ASME